

Spatial gradients and multidimensional dynamics in a neural integrator circuit

Andrew Miri¹, Kayvon Daie^{2,3}, Aristides B Arrenberg^{4,5}, Herwig Baier^{4,5}, Emre Aksay² & David W Tank¹

In a neural integrator, the variability and topographical organization of neuronal firing-rate persistence can provide information about the circuit's functional architecture. We used optical recording to measure the time constant of decay of persistent firing (persistence time) across a population of neurons comprising the larval zebrafish oculomotor velocity-to-position neural integrator. We found extensive persistence time variation (tenfold; coefficients of variation = 0.58–1.20) across cells in individual larvae. We also found that the similarity in firing between two neurons decreased as the distance between them increased and that a gradient in persistence time was mapped along the rostrocaudal and dorsoventral axes. This topography is consistent with the emergence of persistence time heterogeneity from a circuit architecture in which nearby neurons are more strongly interconnected than distant ones. Integrator circuit models characterized by multiple dimensions of slow firing-rate dynamics can account for our results.

Neural integrators are specialized brain circuits that perform the mathematical operation of integration on a time-varying signal¹. This temporal integration is fundamental to a range of motor, memory and decision-making tasks^{2–4}. In the velocity-to-position neural integrator for horizontal eye movements (hVPNI) in the vertebrate oculomotor system, neurons temporally integrate brief eye velocity-encoding burst signals that drive saccades. This integration generates steps in the firing rate of hVPNI neurons that encode an eye position signal necessary for stabilizing gaze^{5,6}. The steps in firing rate of an hVPNI neuron can persist following saccadic input for tens of seconds, ensuring that eye position changes only slowly (decay time constants are typically 10–100 s) during fixations between saccades. The cellular and circuit mechanisms that explain temporal integration and this persistent neural activity remain poorly understood⁷. Understanding these mechanisms in the hVPNI may provide a general framework for understanding temporal integration in other neural systems.

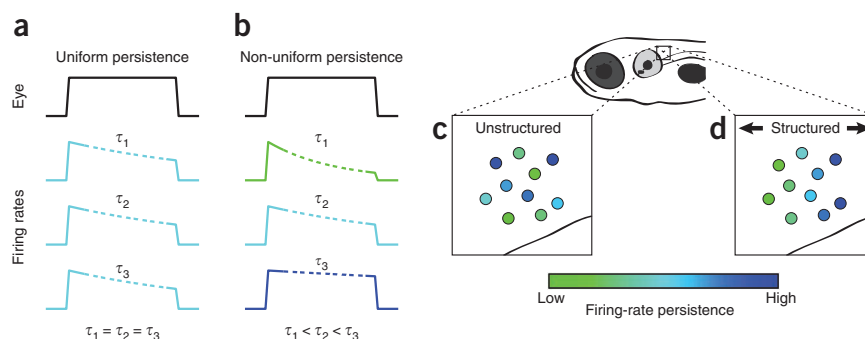
The firing rates of any ipsilateral pair of hVPNI neurons are approximately linearly related to each other over eye positions at which both are active^{8–10}. This observation of the mutual linearity of firing rates led to the idea that the circuit dynamics could be considered as that of a one-dimensional line attractor¹¹. In addition to capturing this linearity, the most commonly considered line attractor-based model of the hVPNI has two other defining characteristics, both of which are aspects of the firing-rate persistence in component neurons following a transient stimulus. First, consistent with experimental observations, the firing rates of neurons in the circuit decay slowly toward a baseline, persisting far longer than typical membrane and synaptic time constants (1–100 ms). Second, this decay is dominated by a single time constant so that the rate of decay is uniform across neurons (Fig. 1a).

Although line attractor dynamics provide a general framework for parametric memory in neural systems^{12,13} and are approximated by several proposed models of the hVPNI^{14–16}, other neuronal circuit architectures have also been proposed. Notably, these architectures make different predictions of firing-rate persistence across the neuronal population. In particular, recurrent network models with circuit architectures or intrinsic neuronal biophysics giving rise to not one, but multiple, long timescales of firing-rate decay have been suggested to be more consistent than line attractor-based models with firing during vestibular stimulation¹⁷ and after detuning^{18,19} and partial inactivation²⁰ of the hVPNI, and may be more robust to perturbation^{11,21}. A circuit exhibiting such multidimensional attractor dynamics could display heterogeneous firing-rate persistence across cells (Fig. 1b). Similarly, recently described integrating circuits that differ from line attractor models by emphasizing feedforward connectivity²² could also display heterogeneous firing-rate persistence across cells, with cells further down the feedforward chain showing progressively longer persistence. Despite its capacity to help distinguish circuit model architectures in terms of the firing dynamics they generate, a systematic experimental study of the similarity of firing-rate persistence across hVPNI neurons has not been reported. This is primarily because simultaneous measurement from many neurons has been difficult in adult preparations studied previously with electrophysiological methods. We recently developed an optical recording-based method for identifying and measuring calcium changes in populations of hVPNI neurons in larval zebrafish²³; these calcium changes can be used to estimate firing-rate dynamics. This created an opportunity to investigate the similarity of persistence times in these populations.

¹Princeton Neuroscience Institute and the Department of Molecular Biology, Princeton University, Princeton, New Jersey, USA. ²Institute for Computational Biomedicine and the Department of Physiology and Biophysics, Weill Cornell Medical College, New York, New York, USA. ³Department of Physics, Cornell University, Ithaca, New York, USA. ⁴Department of Physiology, Programs in Neuroscience, Genetics and Developmental Biology, University of California, San Francisco, San Francisco, California, USA. ⁵Present address: Developmental Biology, Institute Biology I, University of Freiburg, Freiburg, Germany (A.B.A.), Max Planck Institute of Neurobiology, Martinsried, Germany (H.B.). Correspondence should be addressed to D.W.T. (dwtank@princeton.edu) and E.A. (ema2004@med.cornell.edu).

Received 2 May; accepted 27 June; published online 21 August 2011; doi:10.1038/nn.2888

Figure 1 Potential dynamical and spatial structure among hVPNI neurons. (**a,b**) Eye position–dependent firing rates given uniform (**a**) or non-uniform (**b**) firing-rate persistence across neurons. Colored traces show hypothetical firing rates relative to a hypothetical eye position measurement (black). Dotted segments correspond to firing rate during fixation from which firing-rate persistence was measured. (**c,d**) Spatial distribution of neurons in terms of firing-rate persistence given unstructured (**c**) or structured (**d**) arrangements. Cells are pseudocolored according to their firing-rate persistence.



Imaging methods enable not only simultaneous measurement from many neurons that is suitable for examining the diversity of dynamics, but also precise anatomical localization of the recorded cells. Electrophysiological approaches to studying the hVPNI have been limited in resolving the relative locations of neurons from which action potentials were recorded. This has prevented assessment of topography in firing-rate dynamics among hVPNI neurons on short spatial scales ($\leq \sim 100 \mu\text{m}$), yet such structure could also indicate the functional organization of the circuit these neurons comprise. For example, in a neuronal population showing diverse firing-rate persistence, cells could be randomly arranged with respect to this persistence (**Fig. 1c**) or they could be ordered along one or more spatial dimensions (**Fig. 1d**). This sort of order might reflect the time course of neuronal maturation during development²⁴ or differential connectivity between neurons²⁵, as have been observed in other neuronal circuits. Because there is a general relationship between connectivity and circuit dynamics²², characterization of topography could facilitate the understanding of circuit mechanisms underlying neural integration. Observation of structure on these scales in terms of firing patterns could also help to elucidate genetic determination or organization of the hVPNI, as genetically defined cell types can be ordered on short spatial scales^{26,27}.

We measured the variation and spatial organization of firing-rate persistence among hVPNI neurons optically recorded with cellular resolution in awake larval zebrafish during spontaneous eye movements²³. Firing-rate persistence was quantified for these neurons as the persistence time: the time constant of the decay in firing during fixations. Persistence times were measured from cellular fluorescence time series deconvolved with calcium impulse response functions estimated for individual cells from data. These times varied more than tenfold across cells in individual larvae. A corresponding spatial organization on a short length scale ($<100 \mu\text{m}$) was also observed in which persistence times were graded along the rostrocaudal and dorsoventral axes. This spatial organization in functional activity is consistent with a dependence of coupling strength on proximity that results in a circuit architecture ordered in terms of firing-rate persistence.

RESULTS

Identification of eye movement-related hindbrain neurons

We used a recently described²³ optical recording–based method to identify and characterize putative hVPNI neurons in awake larval zebrafish on the basis of the temporal correlation of calcium concentration changes and simultaneously measured eye position (**Fig. 2**). Hindbrain neurons were bolus-loaded with Oregon Green BAPTA-1 AM (OGB-1) and a custom-built two-photon microscope was used to collect image time series from sagittal windows 20–70 μm lateral of the midline that spanned from 100–130 μm to 200–230 μm caudal of the Mauthner cell soma (rhombomere 7/8; **Supplementary**

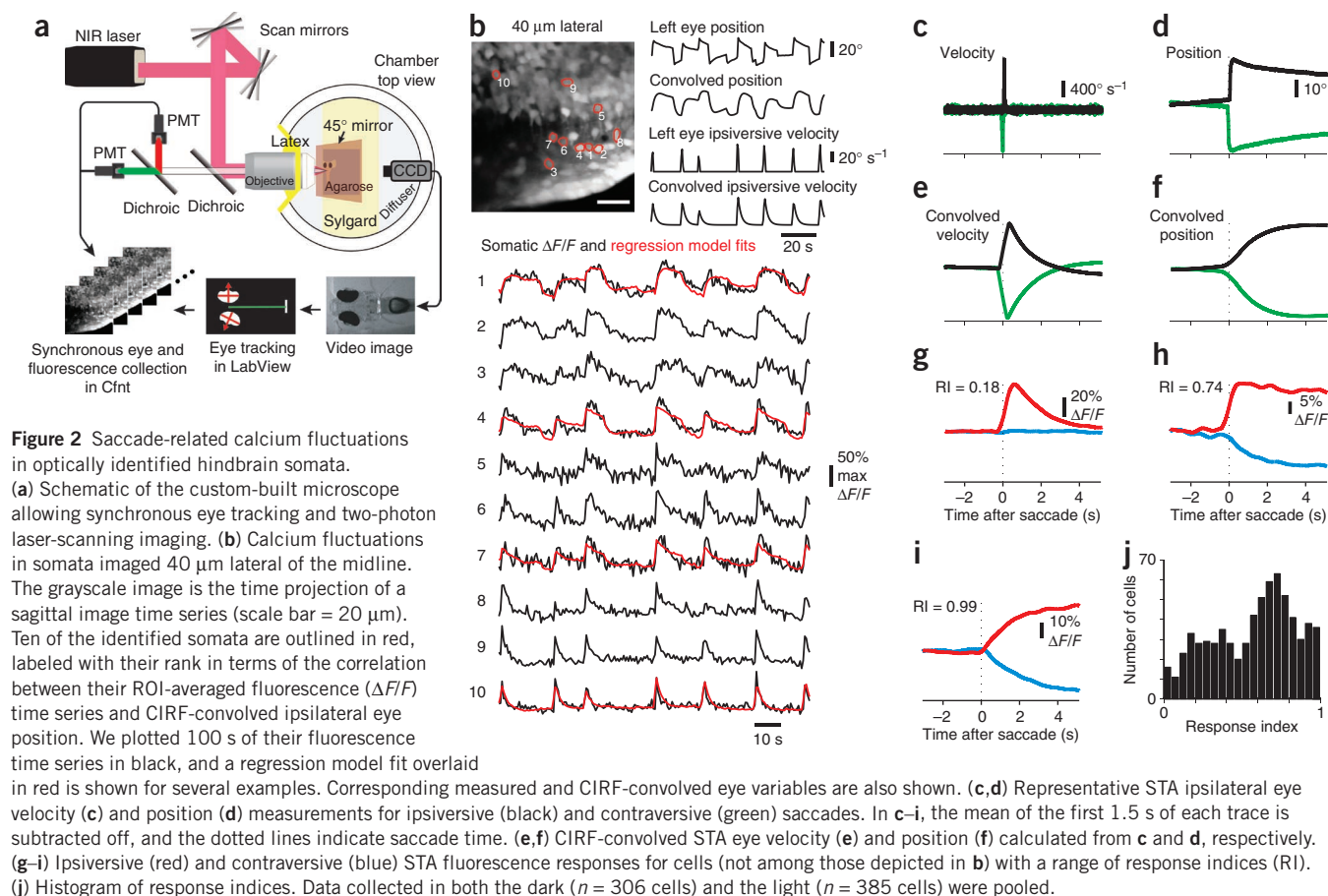
Fig. 1) during spontaneous eye movements (**Fig. 2a**). These imaging windows spanned the lower two-thirds of the dorsoventral extent of the hindbrain. In larval zebrafish, spontaneous eye movements (both in the light and in the dark) frequently consist of a stereotypical back and forth scanning pattern of sequential saccades and fixations. Eye positions are often similar across fixations following saccades in a given direction, producing eye position distributions that are somewhat bimodal. However, we observed gaze stability at multiple eye positions (**Fig. 2b**), indicating that eye position in larval zebrafish is governed by an hVPNI capable of achieving at least an approximate continuum of stable eye positions, rather than just two.

For each ipsiversive saccade and subsequent fixation, ipsilateral eye position–encoding neurons in the caudal hindbrain regions that we imaged, similar to hVPNI neurons in other species, show a burst of action potentials followed by persistent action potential firing at an elevated rate²³. Typically, bursts scale with saccade amplitude (velocity sensitivity), whereas the persistent firing rate scales with eye position (position sensitivity). We found that this firing-rate behavior produced somatic OGB-1 fluorescence time series that could be understood as a sum of ipsilateral eye position and thresholded eye velocity (ipsiversive velocity) convolved with a calcium impulse response function (CIRF) that captures the mapping between action potential firing and intracellular calcium concentration changes. We used CIRFs with the form of an instantaneous increase in calcium followed by an exponential decay. A regression-based approach in which CIRF-convolved eye position and ipsiversive velocity variables serve as regressors in a linear model fit to calcium-sensitive fluorescence image series can be used to identify putative hVPNI neurons in an unbiased way²³. Selection is based on significance measurements of the correlation of each pixel's fluorescence time series with these regressors.

We employed this method to identify hVPNI neurons, focusing all subsequent analysis on somatic regions of interest (ROIs) whose fluorescence time series had a Pearson correlation of greater than 0.5 with either CIRF-convolved eye position or ipsiversive velocity ($n = 691$ identified cells, combined dark and light conditions). Fluorescence time series for example cells showed a clear correspondence with the CIRF-convolved eye position and ipsiversive velocity time series (**Fig. 2b**). We observed a great deal of diversity across cells in the response structure during fixations. Some cells showed relatively stable fluorescence levels during fixations, whereas others showed decaying fluorescence (**Fig. 2b**).

Halorhodopsin-mediated hVPNI localization

Before further analyzing the variability in identified eye movement–related neurons, it was important to determine whether these neurons are part of the hVPNI. We previously found that laser ablation in the hindbrain region imaged here produces deficits in the ability of zebrafish larvae to hold their eyes at eccentric positions²³ without



eliminating saccades. This supports the notion that neurons in this region belong to the hVPNI. In adult preparations, transient pharmacological inactivation has been used to identify the hVPNI^{20,28}. However, such experiments are difficult to perform in a larval nervous system. We therefore used a method for transient optical silencing of neuronal firing analogous to pharmacological inactivation.

We used previously described transgenic zebrafish that express halorhodopsin (NpHR) in most neurons²⁹ to perturb firing in the hindbrain region that we imaged (Fig. 3). A similar method was used previously to localize saccade-generating neurons in rhombomere 5 (ref. 30). We used 633-nm illumination from a low NA optical fiber to focally stimulate NpHR in a column (~200- μm diameter)²⁹ covering the caudal hindbrain (primarily rhombomere 7/8) while also measuring eye position (Fig. 3a,b). Both long (6 s) and short (200 ms) activations markedly reduced eye position stability, causing the eyes to drift rapidly toward the center of gaze (Fig. 3c); centripetal drift was observed regardless of which side of the center the eyes were on before activation (Fig. 3e). The changes induced in eye position were persistent, as the eyes remained at their new positions following the termination of illumination until the subsequent saccade (Fig. 3c). Eye stability was quantified as the slope of linear fits to plots of eye velocity versus eye position (Fig. 3d,e). During illumination, eye positions in NpHR-expressing animals were significantly less stable than those in wild-type larvae ($P = 0.0007$ for short and $P = 0.0015$ for long activations; Fig. 3f), as is observed with pharmacological inactivation of the hVPNI in adults^{20,28}.

On the basis of measurements of the effect of localized optical fiber-based NpHR activation on firing in hindbrain neurons in the strains used for these experiments²⁹, we expect such activation to markedly reduce the average firing rate across these neurons. Our finding that

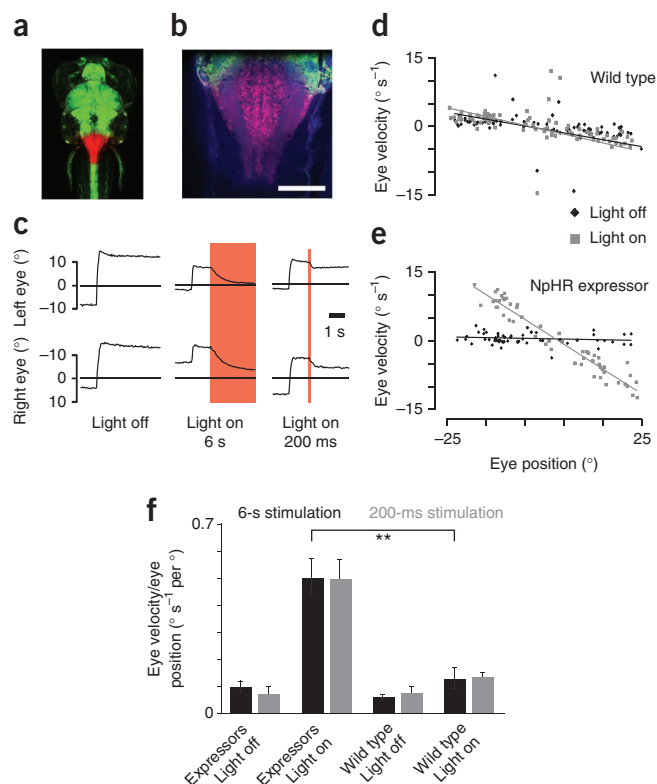
NpHR activation in neurons of the caudal hindbrain diminished gaze stability and permanently altered eye position, when combined with our previous laser ablation results, demonstrates that the neurons that we imaged include the hVPNI.

Distributed firing-rate persistence times

To quantify the dynamics of fluorescence changes, we first computed ipsiversive and contraversive saccade-triggered average (STA) fluorescence responses to represent these changes with an improved signal-to-noise ratio. Only fluorescence measurements surrounding saccades for which the previous saccade was in the opposite direction were included in these averages. This ensured that STAs captured fluorescence changes averaged over repeats of highly similar behaviors. When compared to STA convolved eye velocity (Fig. 2e) and eye position (Fig. 2f), these averages reveal a range of relative ipsiversive velocity and position dependences, from the highly ipsiversive velocity correlated (for example, Fig. 2g) to the highly position correlated (for example, Fig. 2i). Most responses resided between these two extremes (for example, Fig. 2h).

To quantify this variation in relative dependences, we computed a response index for all identified cells (see Online Methods) that is 0 for purely ipsiversive velocity-correlated time series and 1 for purely position-correlated time series (Fig. 2j). Index values varied widely in individual fish; the width of the middle 95% of their distribution in fish ranged from 0.59 to 0.93 in the dark ($n = 6$ larvae with ≥ 18 identified cells) and 0.83 to 0.97 in the light ($n = 6$ larvae with ≥ 18 identified cells). The wide range of sensitivities among cells demonstrated by this distribution is similar to that observed in sequential single-unit recordings of putative hVPNI neurons in cats³¹ and monkeys⁹. Our simultaneous

Figure 3 NpHR-mediated silencing of the caudal hindbrain reduces eye position stability. **(a)** Dorsal view of a 6 dpf larva transgenic for *Et(E1b:Gal4-VP16)s1101t*, *Tg(UAS:NpHR-mCherry)s1989t*, *Tg(UAS:Kaede)s1999t*. The photoconverted region (red) in the caudal hindbrain indicates the volume illuminated in the experiments shown in **c–f**. **(b)** Close-up of the photo-activated region with autofluorescence in blue. Scale bar represents 100 μm . **(c)** Eye traces of the animal in **a** and **b**. Left, a spontaneous saccade without illumination. Middle, NpHR was activated in the caudal hindbrain 1 s after a spontaneous saccade (red shade). The eyes drifted back toward the center of gaze. Right, short NpHR activation (red shade) induced transient eye drift. **(d,e)** Position-velocity plots for 200-ms illumination experiments with least-squares best fit lines of slope k . **(d)** No substantial eye velocity increase was observed in a wild-type animal during illumination (light on, $k = -0.19$; light off, $k = -0.15$). **(e)** Illumination of the hindbrain in the NpHR-expressing animal shown in **a** induced large increases in eye velocity across eye positions (light on, $k = -0.54$; light off, $k = -0.02$). **(f)** Quantification of k across animals ($n = 4–5$ each). **indicate a statistically significant difference ($P = 0.0007$ for short and $P = 0.0015$ for long activations). Error bars represent s.e.m.



measurements of activity in many cells confirm that such heterogeneity is characteristic of population activity in the hVPNI.

Because the fixations typical in our larval preparation are long (generally >5 s), we were able to use OGB-1 STA fluorescence responses to examine the uniformity of firing-rate persistence across many identified hVPNI neurons in individual larvae. Our strategy was to first compute STA firing-rate estimates from STA fluorescence responses by deconvolving fluorescence responses with the CIRF determined individually for each cell (Supplementary Fig. 2). The CIRF decay time constant, τ , was calculated for each neuron from an analysis of the fluorescence decay following contraversive saccades²³ (see Online Methods). This analysis was limited to cells whose fluorescence had a Pearson correlation greater than 0.5 with CIRF-convolved eye position ($n = 455$ position cells) to include only cells having robust persistent activity and further to cells with CIRF τ estimates of reasonable quality ($R^2 > 0.5$, $n = 416$).

The estimated firing rate for most cells appeared to decay over several seconds during fixation toward a baseline level associated with the center of gaze. However, across cells in individual fish, STA firing-rate estimates displayed extensive variation in the rate of this decay, and thus in the degree of firing-rate persistence. To quantify this persistence, we used time constants from exponential fits to firing-rate estimates to measure persistence time (Fig. 4a,b and Supplementary Fig. 3; see Online Methods). Because of some ambiguity in CIRF τ and the baseline

level to which firing-rate estimates decay, each estimate is consistent with a distribution of persistence times. We refer here to the extent of the middle 99% of this distribution as the persistence time range.

Because the canonical line attractor model predicts that persistence times among hVPNI neurons would be similar (Fig. 1a), we sought explicit evidence for non-overlapping persistence time ranges in individual larvae. Several non-overlapping persistence time ranges were observed in each larvae both in the dark ($n = 5$ larvae with ≥ 16 position cells) and the light ($n = 5$ larvae with ≥ 19 position cells), consistent with the presence of multiple distinct persistence times across cells in individual fish. For each larva, persistence time distributions were statistically unlikely to be drawn from a single underlying distribution (Kruskal-Wallis test, $P < 10^{-10}$ for each larvae, $n = 5$ in the dark and $n = 5$ in the light). The median values from

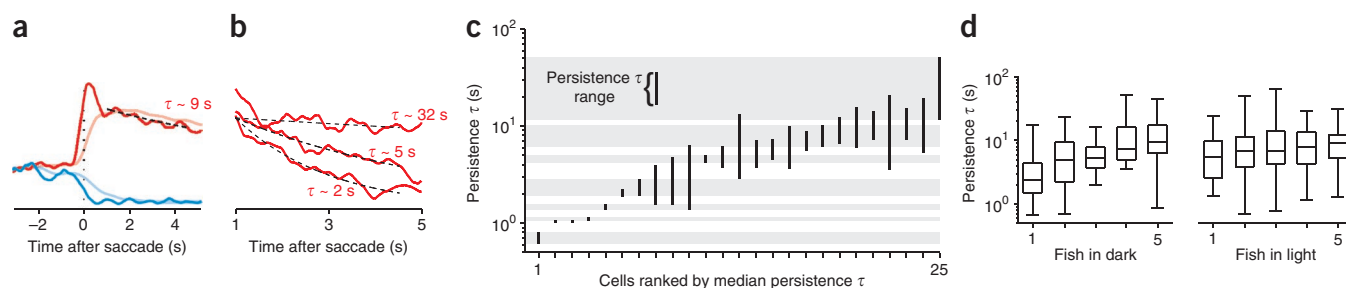


Figure 4 The distribution of persistence time ranges in individual larvae. **(a)** Representative ipsiversive (red) and contraversive (blue) STA fluorescence responses, before (translucent) and after (opaque) deconvolution with a CIRF. The mean of the first 1.5 s of each trace is subtracted off. The black dashed line is the fit of an exponential function ($\tau = 9.26$ s) to the deconvolved ipsiversive STA response from 1 to 4.5 s after saccade time. **(b)** Ipsiversive STA fluorescence responses from three cells in one fish from 1–5 s after saccade time. Black dashed lines show exponential fits with time constants indicated. Traces are normalized to the value of the fit 1 s after saccade time. **(c)** Persistence time ranges for 25 cells imaged in one fish in the dark. The vertical extent of each bar spans the persistence time range for each cell. The gray bars span the ranges for seven cells for which the ranges do not overlap. Cells are ordered according to their rank in terms of the median of their persistence time distribution. **(d)** Box plots representing the distribution of median persistence times for fish imaged in the dark (left) or the light (right). Horizontal lines indicate the minimum, 25th percentile, median, 75th percentile and maximum values of each distribution.

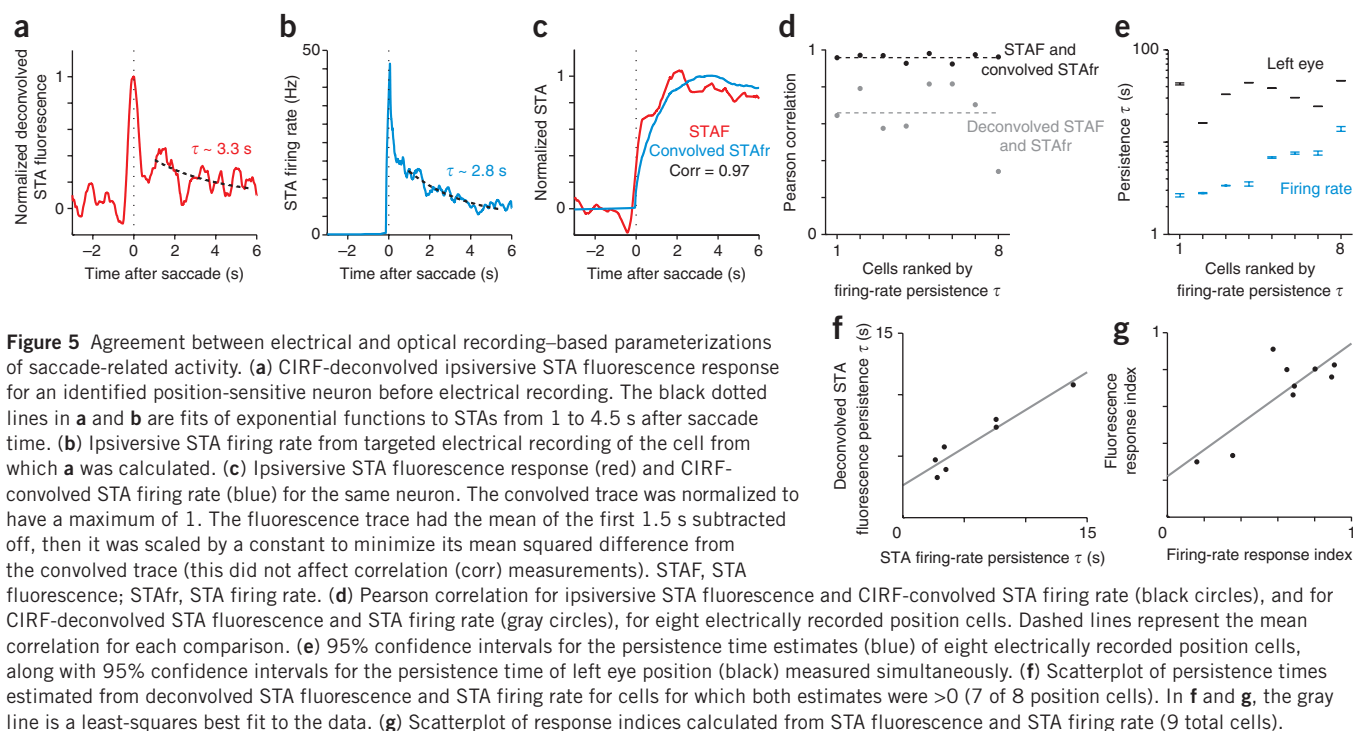


Figure 5 Agreement between electrical and optical recording-based parameterizations of saccade-related activity. **(a)** CIRF-deconvolved ipsiversive STA fluorescence response for an identified position-sensitive neuron before electrical recording. The black dotted lines in **a** and **b** are fits of exponential functions to STAs from 1 to 4.5 s after saccade time. **(b)** Ipsiversive STA firing rate from targeted electrical recording of the cell from which **a** was calculated. **(c)** Ipsiversive STA fluorescence response (red) and CIRF-convolved STA firing rate (blue) for the same neuron. The convolved trace was normalized to have a maximum of 1. The fluorescence trace had the mean of the first 1.5 s subtracted off, then it was scaled by a constant to minimize its mean squared difference from the convolved trace (this did not affect correlation (corr) measurements). STAF, STA fluorescence; STAFr, STA firing rate. **(d)** Pearson correlation for ipsiversive STA fluorescence and CIRF-convolved STA firing rate (black circles), and for CIRF-deconvolved STA fluorescence and STA firing rate (gray circles), for eight electrically recorded position cells. Dashed lines represent the mean correlation for each comparison. **(e)** 95% confidence intervals for the persistence time estimates (blue) of eight electrically recorded position cells, along with 95% confidence intervals for the persistence time of left eye position (black) measured simultaneously. **(f)** Scatterplot of persistence times estimated from deconvolved STA fluorescence and STA firing rate for cells for which both estimates were >0 (7 of 8 position cells). In **f** and **g**, the gray line is a least-squares best fit to the data. **(g)** Scatterplot of response indices calculated from STA fluorescence and STA firing rate (9 total cells).

persistence time distributions varied by approximately an order of magnitude or more in individual larvae, both in the dark and in the light (Fig. 4c,d and Supplementary Fig. 4a). The width of the middle 95% of the distribution of these medians in larvae ranged from 13.41 to 48.00 s in the dark ($n = 5$) and 21.63 to 62.76 s in the light ($n = 5$). The shape and width of these distributions of medians were not sensitive to the choice of thresholds for data inclusion (Supplementary Table 1). The coefficient of variation for these distributions of medians ranged from 0.58 to 0.94 in the dark ($n = 5$) and 0.70 to 1.20 in the light ($n = 5$).

The presence of multiple distinct persistence times in individual larvae was further illustrated by average STA firing-rate estimates for cells grouped according to median persistence time (Supplementary Fig. 5). Persistence time heterogeneity was still observed if firing-rate estimates were calculated for all cells with a single CIRF instead of CIRFs for which τ was determined cell specifically (Supplementary Fig. 5g–i).

We validated the finding of persistence time heterogeneity using a second approach in which a function modeling the convolution of underlying firing with a CIRF was fit directly to STA fluorescence responses (see Online Methods). This approach yielded similar heterogeneity in persistence time estimates (Supplementary Fig. 4b). Although single exponential decays did not capture all of the structure in ipsiversive STA firing-rate estimates (Supplementary Fig. 6a), they adequately captured the magnitude of firing-rate decay during fixation, which is sufficient to reveal heterogeneity in persistence time across cells. Similar heterogeneity was also observed via a different metric of persistence time, the fractional change of STA firing-rate estimates during fixation (Supplementary Fig. 6b). The presence of multiple distinct persistence times is inconsistent with neural integrator models characterized by uniform firing-rate persistence across cells, such as the canonical line attractor-based circuit model.

Validation of fluorescence-based firing rate estimates

To confirm that persistence time estimates from fluorescence reflect the actual dynamics of action potential firing, we compared these

estimates with persistence times determined from electrical recordings from the same cell (Fig. 5). Following image time series acquisition, we made single-unit loose-patch recordings from cells that we identified using our online regression-based strategy²³. Persistence times were calculated for recorded neurons both from deconvolved STA fluorescence (Fig. 5a) and STA firing rates (Fig. 5b). The correlation between deconvolved STA fluorescence responses and STA firing rates was strong (Fig. 5a,b,d). Similarly, the CIRF-convolved STA firing rate was highly correlated with STA fluorescence (Fig. 5c,d). The somewhat lower correlation for deconvolved STA fluorescence and STA firing rate is likely a result of the amplification of noise in fluorescence measurements upon deconvolution.

Persistence times calculated from STA firing rates ranged from 2.65 to 13.87 s ($n = 8$; Fig. 5e). The correlation between these values and persistence times calculated in a similar fashion for the simultaneously measured ipsilateral (left) eye position was 0.30, suggesting that only a small amount (~10%) of the variance in persistence times can be explained by variation in the stability of the eyes themselves. This fact, coupled with the greater than fivefold difference between the shortest and longest persistence times is itself strong evidence of heterogeneity in firing-rate persistence across hVPNI cells. Moreover, persistence times estimated from fluorescence and firing rate for the same neurons showed strong agreement (slope = 0.62, $R^2 = 0.91$, r.m.s. error = 0.88 s; Fig. 5f). These results confirm that the distribution of persistence times measured from STA fluorescence responses reflects a similar distribution of persistence times for the underlying firing rates.

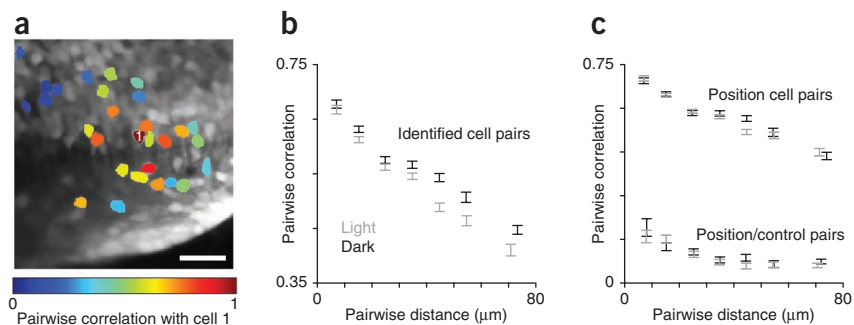
An analogous validation was performed for response indices. Correlations between the firing-rate time series and the time series of both eye position and ipsiversive velocity were used to calculate a firing rate-based response index for recorded neurons. These values were consistent with response indices calculated from fluorescence for the same neurons (slope = 0.77, $R^2 = 0.69$, r.m.s. error = 0.13; Fig. 5g). This suggests that fluorescence-based response indices report relative burst and position sensitivities in firing rates with an accuracy that is sufficient to conclude that

Figure 6 Activity correlations between cells depend on their pairwise distance.

(a) Time projection of an image time series with 29 identified neurons color-coded according to the Pearson correlation of their fluorescence time series with that of the cell labeled '1'. Scale bar represents 20 μm .

(b) Pairwise correlation of fluorescence time series for pairs of identified cells versus pairwise distance for data collected in the light (gray) and in the dark (black). (c) Pairwise correlation of fluorescence time series for position cell pairs and position/control cell pairs versus pairwise distance for data collected in the light (gray) and in the dark (black).

For the plots in **b** and **c**, pairs were grouped according to pairwise distance, data are plotted along the x axis according to the mean pairwise distance for each group and error bars represent mean \pm s.e.m.



the distribution of response indices we observed corresponds to a distribution of relative sensitivities in firing rates.

Spatial gradients of persistence time and response index

In addition to providing measurements of activity from many cells simultaneously, optical recording identifies the precise anatomical location of each recorded cell. We used this information to examine whether the variation in saccade-related firing presented above corresponded to a topographic organization among neurons. Topography was observed in terms of three quantities: correlation between fluorescence time series, firing-rate persistence time and response index.

The Pearson correlation for fluorescence time series was calculated for all pairs of identified cells in individual image time series. When the correlation with a particular cell was plotted using color-coded somata for all other identified cells (this included position cells and those that may be exclusively ipsiversive velocity sensitive) nearby cells appeared to be more highly correlated (Fig. 6a). When the data from all image time series were combined, pairwise correlation was significantly negatively correlated with the distance separating the cells (pairwise distance) in three dimensions both in the dark and light (in the dark, Spearman rank correlation

(src) = -0.36 , $P < 10^{-9}$; in the light, src = -0.33 , $P < 10^{-9}$; Fig. 6b). The same held true for pairs of position cells (in the dark, src = -0.36 , $P < 10^{-9}$; in the light, src = -0.34 , $P < 10^{-9}$; Fig. 6c). Significant dependence of pairwise correlation among position cells was seen for pairwise distance along both the rostrocaudal (in the dark, src = -0.29 , $P < 10^{-9}$; in the light, src = -0.24 , $P < 10^{-9}$) and dorsoventral (in the dark, src = -0.23 , $P < 10^{-9}$; in the light, src = -0.27 , $P < 10^{-9}$) axes.

To rule out the possibility that these correlations stemmed from specimen motion-induced correlations or fluorescence from processes overlapping cellular ROIs out of the image plane, we examined the proximity dependence of the correlation between position cells and a control population of non-position-dependent cells (absolute value of Pearson correlation with CIRF-convolved eye position < 0.15). Pairs of position and control cells showed pairwise correlations that were weakly distance dependent at short distances, but were not significantly dependent on distance beyond 35 μm (Fig. 6c). For position/control cell pairs $\geq 35 \mu\text{m}$ apart, the src of pairwise correlation and pairwise distance was -0.02 ($P = 0.60$) in the dark and -0.02 ($P = 0.50$) in the light. However, for position cell pairs $\geq 35 \mu\text{m}$ apart, the src of pairwise correlation and pairwise distance was -0.29 ($P < 10^{-9}$) in the dark and -0.16 ($P < 10^{-9}$) in the light. These results suggest that the proximity dependence of correlation between identified position neurons is unlikely to be explained by motion-induced fluorescence correlations or overlapping processes.

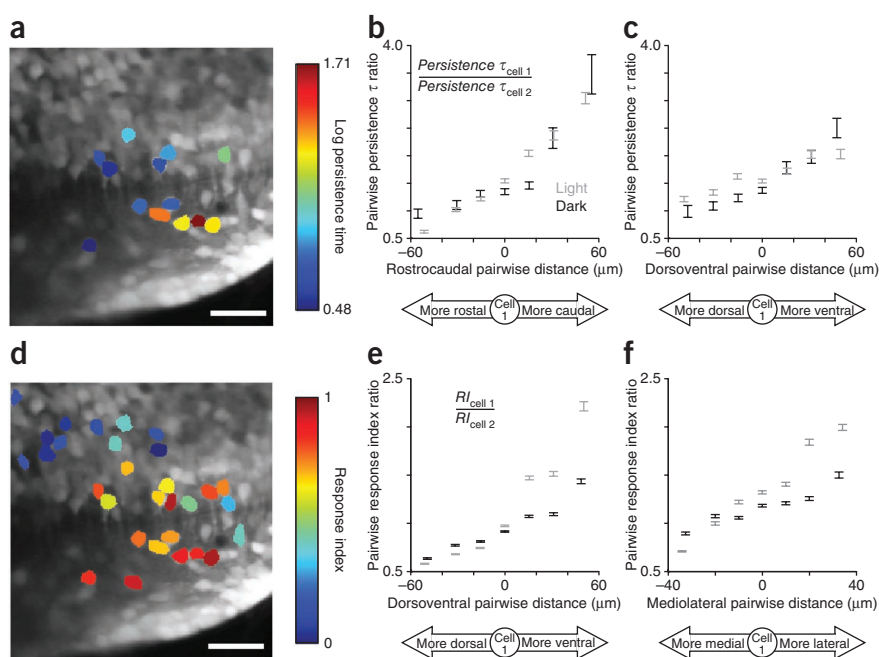


Figure 7 Persistence time and response index similarity depend on pairwise distance along spatial dimensions. (a) Time projection of an image time series with 13 position neurons color-coded according to the \log_{10} of their persistence time. Scale bars in **a** and **d** represent 20 μm . (b,c) Persistence time ratio versus pairwise distance along the rostrocaudal (b) and dorsoventral (c) axes for pairs of position neurons. Data are included from cells for which persistence time estimates were > 0 . For the plots in **b**, **c**, **e** and **f**, pairs identified in the light (gray) or dark (black) were grouped according to pairwise distance along particular spatial dimensions, data are plotted along the x axis according to the mean pairwise distance for each group and error bars represent mean \pm s.e.m. (d) Time projection of the same image time series with 29 identified neurons colored-coded according to their response index. (e,f) Response index ratio versus pairwise distance along the dorsoventral (e) and mediolateral (f) axes for pairs of identified neurons.

Topography was also seen among cells in terms of persistence time. Notably, we observed gradients of persistence time along spatial dimensions. For pairs of position cells, we quantified the similarity between persistence times using their ratio. To introduce directionality, we set the ratio's denominator as the value for the cell relative to which pairwise distance was measured. We found a clear dependence of this ratio on pairwise distance along individual spatial dimensions (Fig. 7a–c and Supplementary Fig. 7a). The srcs of this persistence time ratio with rostrocaudal, dorsoventral, and mediolateral distance were 0.22, 0.28 and 0.06 in the dark, respectively, and 0.35, 0.11 and –0.21 in the light, respectively. The magnitude of these correlation values depended only weakly on the choice of thresholds for data inclusion (Supplementary Table 2). The dependence was most prominent across both dark and light conditions along the rostrocaudal axis (Fig. 7a,b and Supplementary Figs. 8 and 9). In the dark, higher persistence time cells tended to be located more caudally and ventrally than lower persistence time cells.

Response index similarity had a somewhat different spatial dependence across all of the identified cells (Fig. 7d–f and Supplementary Fig. 7b). The response index ratio varied most prominently over the dorsoventral and mediolateral axes. The srcs of response index ratio with rostrocaudal, dorsoventral and mediolateral distance were 0.05, 0.30 and 0.19 in the dark, respectively, and –0.10, 0.45 and 0.32 in the light, respectively.

DISCUSSION

We report two major findings on the functional organization of the hVPNI. First, our optical recordings reveal a heterogeneity in firing-rate persistence. Second, we observed that persistence times were graded along the rostrocaudal and dorsoventral axes, implying that cells with similar persistence times tended to be closer together in space. To the best of our knowledge, this is the first elucidation of functional organization in a neuronal circuit subserving temporal integration or parametric short-term memory in general on a length scale smaller than 100 μm .

We also report advances in methodology. The heterogeneity that we observed in relative position and ipsiversive velocity sensitivity is consistent with findings from electrode studies in adult vertebrates, supporting larval zebrafish as a model for investigating the mechanisms and development of neural integration. In addition, the correspondence demonstrated between electrode recordings and CIRF-deconvolved optical recordings establishes that the latter can be a reliable reporter of collective neuronal dynamics.

To explain the apparent continuum of stable eye positions observed during fixations in adult vertebrates, hVPNI firing-rate dynamics have been modeled as approximating a line attractor^{11,14}. In a state space in which each axis represents one neuron's firing rate, a line attractor is a continuous line of stable points, each representing the set of firing rates corresponding to one horizontal eye position (see Figure 1 in ref. 11). This line represents the continuum of eye positions possible during fixations. Both eye position and hVPNI neuronal firing rates are observed to slowly drift centripetally during fixations, suggesting that positions along the line are only semi-stable, with the circuit's representation in state space drifting slowly along the line toward a single fixed point corresponding to the center of gaze. The firing of all hVPNI neurons would then decay at a uniform rate (Fig. 8a,b), implying that the circuit dynamics are one dimensional. However, we observed hVPNI neuron firing decaying on multiple timescales (Fig. 8c), inconsistent with the line attractor model as originally formulated¹¹ and directly demonstrating that the dynamics are multidimensional.

Previous studies of the adult hVPNI have not systematically examined the uniformity of firing-rate drift dynamics across neurons

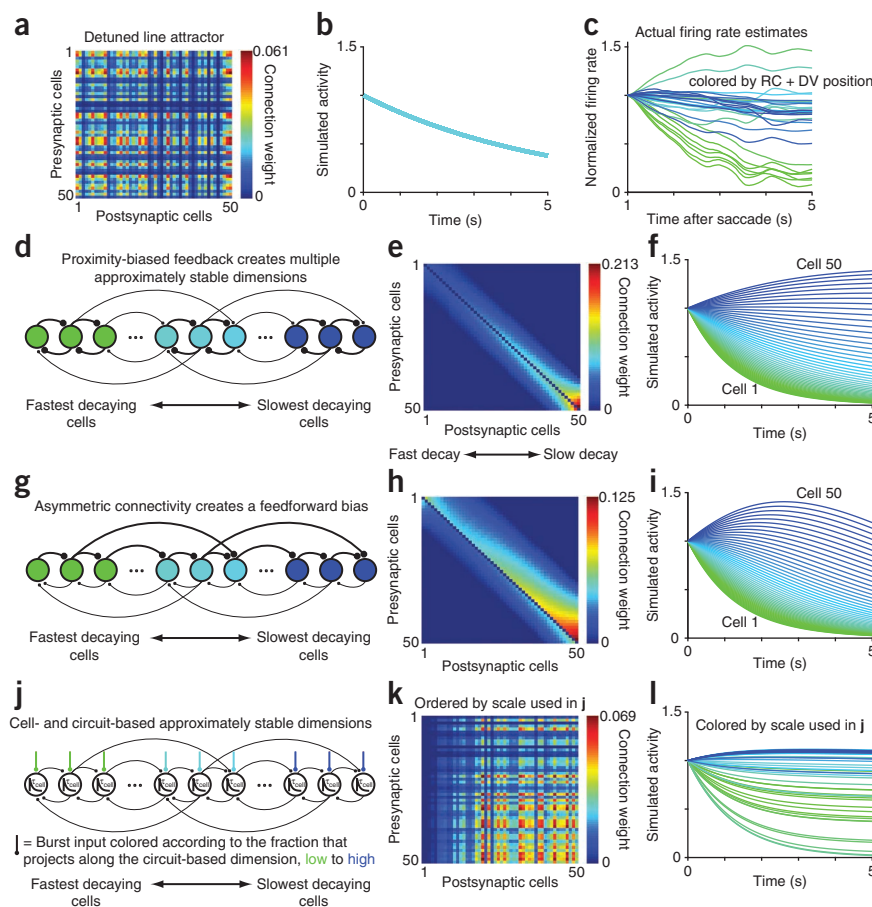
during fixations. Our discovery of persistence heterogeneity was facilitated by optical recording, which provided simultaneous activity measurements from groups of hVPNI neurons. Heterogeneity could also be masked in adults by the fact that persistence times increase while the duration of individual fixations decreases, making it more challenging to observe and then quantify differences across neurons. However, a wide range of persistence times (~4 s to –21 s) from cells measured across many adult goldfish has been reported¹⁸. These measurements were not simultaneous, and bounding these estimates or quantifying their relationship to variation in integrator performance across fish would be required for a direct comparison with our results. The authors further found extensive evidence of persistence heterogeneity in sequential electrode recordings in goldfish whose hVPNI were detuned via erroneous visual feedback¹⁸. The larval zebrafish that we examined showed fixation stability similar to that of a somewhat detuned adult, raising the possibility that persistence heterogeneity becomes less prominent in a properly tuned adult hVPNI. This would imply that the persistence time distribution may narrow during development.

Exploring this idea quantitatively, we re-analyzed previously published simultaneous recordings from pairs of adult goldfish hVPNI neurons during spontaneous eye movements³² to estimate the percent difference in persistence time between each pair. The median percent difference was 34% ($n = 6$ ipsilateral pairs). We then calculated the percent difference between persistence times for pairs of simultaneously imaged zebrafish neurons and found a median percent difference of 69% ($n = 1,576$ ipsilateral pairs). The two datasets were statistically unlikely to be drawn from a common distribution (Wilcoxon test, $P = 0.048$). Our results suggest that some persistence heterogeneity exists in adult goldfish and that larval heterogeneity may be comparatively more exaggerated. However, a more systematic characterization of adult persistence times would be necessary to directly compare larval and adult persistence time distributions.

Persistence time heterogeneity is consistent with other findings in adults beyond those mentioned above, further supporting its existence in the adult hVPNI. First, during sinusoidal vestibular stimulation, the dependence on stimulus frequency of putative hVPNI neurons' firing phase relative to eye position^{9,33} is captured by models in which cells show non-uniform firing rate decay^{17,34}. Second, hysteresis in the dependence between firing rates of hVPNI neurons during fixation is inconsistent with canonical line attractor dynamics³⁵, but would be expected if multiple timescales of decay were present to varying degrees in these firing rates. Third, the results of experiments on monocular optokinetic stimulation point to a lack of uniformity in firing dynamics across hVPNI neurons³⁶. Finally, evidence for a broad distribution of relaxation times in the eye plant³⁷ suggests that diverse persistence times in hVPNI neurons could contribute to gaze stabilization. Optimal control of such a plant would necessitate neuronal drive to eye muscles with a similar distribution of relaxation times to stabilize gaze; this could be provided by appropriately patterned innervation of motor neurons from hVPNI neurons with different persistence times.

The topography of hVPNI neuronal persistence that we observed on length scales smaller than 100 μm has not been previously reported; however, the poor spatial resolution of electrode recording would preclude characterization of topography on this scale. The response index gradients that we found are analogous to the rostrocaudal gradients in relative position and velocity sensitivity seen among hVPNI neurons in cats³¹, although similar organization was not observed among goldfish hVPNI neurons¹⁰. Looking on a shorter length scale, we did not see a prominent rostrocaudal

Figure 8 Mechanistic implications of heterogeneity in dynamics. **(a,b)** Connectivity matrix **(a)** and numerical simulation results **(b)** for a circuit constructed to generate a line attractor, then subjected to uniform detuning of connection weights to achieve a persistence time of ~5 s (approximately the median for the cells from which we estimated this quantity). The traces in **b**, which all overlap, show the time courses for 50 neurons from simulations. **(c)** Firing rate estimates for 29 neurons imaged in one larvae in the dark. Saccade-triggered fluorescence was smoothed by projection onto principal components capturing >99% of the variance in the data before deconvolution. Traces are colored according to the sum of the rostrocaudal and dorsoventral (RC + DV) location of each neuron, revealing again the correspondence between persistence time and location along these dimensions. **(d)** Recurrent feedback circuit in which neurons nearby in space with more similar persistence times are more strongly coupled. This generates multiple approximately stable dimensions in firing-rate state space. The colors of cells in **d** and **g** correspond to the colors of simulation results in **f** and **i**, respectively. **(e,f)** Connectivity matrix **(e)** and numerical simulation results **(f)** for a network constructed with the features shown in **d**. Cells are ordered in **e** and **h** from 1 to 50 in order of increasing persistence. **(g)** Asymmetric recurrent connectivity with a feedforward bias. Strong local coupling creates an ordering in which the activity of cells is more persistent further down the feedforward chain partially as a result of progressive input filtration. **(h,i)** Connectivity matrix **(h)** and numerical simulation results **(i)** for a network constructed with the features shown in **g**. **(j)** Cell-intrinsic processes generate one timescale of persistence (τ_{cell}) and tuned recurrent feedback generates another. By tuning the inputs to cells to differentially express these two timescales, a continuum of apparent persistence times can be achieved. **(k,l)** Connectivity matrix **(k)** and numerical simulation results **(l)** for a network constructed with the features shown in **j**. Cells are ordered in **k** from 1 to 50 and colored in **l** according to the fraction of their burst input that projects along the circuit-based dimension, from lowest to highest.



gradient in relative sensitivity, but we did see a strong dependence of persistence time along this dimension.

The topography that we observed may reflect developmental patterning in the nascent hVPNI circuit. A recent study found that older cells reside more ventrally in the caudal hindbrain³⁸ during early larval stages, suggesting that relative position sensitivity and persistence time may increase with neuronal age during these stages. This could reflect synaptic input tuning that improves firing-rate persistence as neurons mature. This study also found that neuropil clusters according to neuronal age in the hindbrain³⁸. This clustering may increase the connectivity likelihood for similarly aged neurons, thereby increasing this likelihood for neurons with similar persistence. Such clustering could contribute to a proximity bias in connectivity likelihood that may explain the spatial gradients we observed. Spatial gradients in the anatomical position of spinal motor neurons and premotor interneurons subserving fast and slow swimming have also been reported in the larval zebrafish^{24,39}. Our observations add to the evidence that spatial gradients in the dynamical properties of neurons in circuits may be a general property of anatomical organization in the developing vertebrate CNS. Although continued migration may alter the spatial arrangement of cells, the synaptic connections forged during development can contribute to the functional organization of adult circuits.

In general, correlation-proximity relations can be ascribed to convergent afferent input. However, in the hVPNI, saccadic burst input is transient, sustained vestibular input is not eye position dependent^{40,41}, and persistent firing encoding eye position must emerge locally via recurrent excitation and/or cell-intrinsic mechanisms²⁰. Convergent afferent input from neurons external to the hVPNI does not seem a tenable explanation. However, if a new source of eye position feedback to the caudal hindbrain was discovered, convergent input would warrant reconsideration.

Persistence heterogeneity is consistent with hVPNI circuit models that are dynamically distinct from the canonical line attractor model. The classic line attractor exhibits one approximately stable dimension in firing-rate state space along which firing rates change slowly, whereas persistence heterogeneity requires mechanisms generating slow firing-rate dynamics along multiple dimensions. Notably, integrator models with slow dynamics along multiple dimensions will be more robust than line attractor-type models to local perturbations of the circuit, such as the loss of a neuron^{11,21}.

One possibility is that locally biased synaptic feedback among hVPNI neurons generates a multidimensional attractor with several approximately stable dimensions (Fig. 8d). Simulations of such a model can produce persistence time distributions that are qualitatively similar to those that we observed experimentally (Fig. 8e,f).

Here, the variation in persistence emerges from structured connectivity in which cells with more similar (disparate) persistence times tend to be more strongly (weakly) coupled. If the spatial gradients that we observed emerge from a proximity bias in the likelihood any two neurons are connected, they would imply exactly this type of circuit structure.

A second possibility is that persistence heterogeneity arises by a progressive filtering of activity propagating down a feedforward cascade²². Such circuits need not be purely feedforward, and may involve a mixture of feedback and feedforward connections or even functionally feedforward interactions. An example of a circuit using feedforward dynamics is shown in **Figure 8g**, where locally biased synaptic connectivity is modified with a feedforward bias, generating firing rate dynamics that resemble those seen in our data (**Fig. 8h,i**). In general, the activity of all neurons in this circuit type eventually decreased during simulated fixations if the contribution of feedforward activity was substantial. Further work would be needed to address whether this circuit type is capable of generating persistence on longer timescales when the number of neurons is on the order that we considered.

A third possibility is that two distinct timescales of firing-rate decay are generated separately by recurrent feedback and a cell-intrinsic mechanism (**Fig. 8j**). Previous results following partial inactivation of the goldfish hVPNI are consistent with the presence of a cell-intrinsic mechanism generating 1–2-s firing-rate persistence. Differential manifestation across cells of this persistence and a longer timescale persistence resulting from recurrent feedback could create varying persistence times. The topography we observed would then suggest that saccadic burst input to the hVPNI is spatially structured to vary the degree to which each timescale dictates a cell's persistence. Simulations demonstrated that such a model can recapitulate spatially graded persistence heterogeneity (**Fig. 8k,l**).

Recent theoretical results have shown that randomly connected recurrent networks with heterogeneous unit activity can execute functional transformations such as temporal integration^{19,42}. Investigating such networks may identify other circuit architectures that can generate the firing dynamics we observed. In general, although our measurements in larvae expose a multidimensional firing dynamics that can reconcile a number of observations from adults, the precise hVPNI circuit architecture instantiating these dynamics remains unknown. Emerging techniques for comprehensive connectivity reconstruction could further these efforts⁴³.

hVPNI neurons must by definition have eye position-dependent firing, and eye position, but not saccades themselves, must causally depend on that firing. Previous results have shown that laser ablation in the caudal hindbrain region studied here, which contains neurons with position-dependent firing, reduces gaze stability²³. We found that NpHR-mediated perturbation of firing in an ~200- μ m diameter focal area encompassing the same region induced rapid centripetal drift in eye position, causing position changes that persisted following termination of NpHR activation. These complementary results localize hVPNI functionality to neurons in this hindbrain region.

An important question is whether all of the neurons that we designated as position cells and for which we estimated persistence times belong to the hVPNI. We expect few if any of our position cells to be exclusively ipsiversive velocity sensitive, similar to saccadic burst neurons, as electrical recordings from cells meeting our criteria for classification as position cells revealed eye position-dependent firing in all cases²³. We further expect the fraction of designated position cells participating instead in the velocity storage integrator to be very low. Neurons in this integrator show firing that depends only

weakly on eye position during spontaneous eye movements in adult goldfish⁴⁴ and its anatomical location in larval zebrafish⁴⁵ overlaps minimally with the region that we imaged.

Assuming that NpHR activation directly hyperpolarizes hVPNI neurons rather than just their tonic inputs (as is suggested by centripetally drifting exponential relaxation in eye position), the effects of NpHR activation are inconsistent with some hypothesized cell-intrinsic neural integration mechanisms. Although circuit mechanisms of integration have been strongly implicated in the hVPNI^{20,46,47}, a contribution from cell-intrinsic mechanisms cannot be excluded⁷. In contrast to proposed membrane voltage-independent mechanisms^{48–50}, the persistent change of firing in hVPNI neurons following the transient hyperpolarization that we observed suggests that both cellular and circuit contributions to integration are membrane-voltage dependent. Further studies using optogenetic probes to perturb activity in hVPNI neurons could be fruitful in elucidating the cellular and circuit mechanisms underlying neural integration in the hVPNI.

METHODS

Methods and any associated references are available in the online version of the paper at <http://www.nature.com/natureneuroscience/>.

Note: Supplementary information is available on the Nature Neuroscience website.

ACKNOWLEDGMENTS

We thank D. Dombeck for technical advice, F. Collman for motion-correction software, and M. Goldman, A. Kinkhabwala and P. Bradley for helpful discussions. This work was supported by a National Science Foundation predoctoral fellowship (A.M.), a US National Institutes of Health Training grant (EY007138-16, K.D.), a Krevans fellowship (A.B.A.), a Burroughs-Wellcome Career Award at the Scientific Interface, a Searle Scholar award, the Frueauff Foundation (E.A.), the Human Frontier Science Program (H.B.), and US National Institutes of Health grants (R01 MH060651 to D.W.T. and R01 NS053358 to H.B.).

AUTHOR CONTRIBUTIONS

A.M. collected functional imaging and electrical recording data under the supervision of D.W.T.; A.M., E.A. and D.W.T. developed the preparation, experimental procedures and instrumentation for the imaging and electrophysiological studies; A.M. and K.D. analyzed this data with guidance from E.A. and D.W.T.; A.B.A. and H.B. designed the NpHR study; A.B.A. collected and analyzed the NpHR data; and A.M., K.D., E.A. and D.W.T. wrote the paper.

COMPETING FINANCIAL INTERESTS

The authors declare no competing financial interests.

Published online at <http://www.nature.com/natureneuroscience/>.

Reprints and permissions information is available online at <http://www.nature.com/reprints/index.html>.

- Robinson, D.A. Integrating with neurons. *Annu. Rev. Neurosci.* **12**, 33–45 (1989).
- Oestreich, J., Dembrow, N.C., George, A.A. & Zakon, H.H. A "sample-and-hold" pulse-counting integrator as a mechanism for graded memory underlying sensorimotor adaptation. *Neuron* **49**, 577–588 (2006).
- Huk, A.C. & Shadlen, M.N. Neural activity in macaque parietal cortex reflects temporal integration of visual motion signals during perceptual decision making. *J. Neurosci.* **25**, 10420–10436 (2005).
- Taube, J.S. & Bassett, J.P. Persistent neural activity in head direction cells. *Cereb. Cortex* **13**, 1162–1172 (2003).
- Cohen, B. & Komatsuzaki, A. Eye movements induced by stimulation of the pontine reticular formation: evidence for integration in oculomotor pathways. *Exp. Neurol.* **36**, 101–117 (1972).
- Skavenski, A.A. & Robinson, D.A. Role of abducens neurons in vestibuloocular reflex. *J. Neurophysiol.* **36**, 724–738 (1973).
- Major, G. & Tank, D. Persistent neural activity: prevalence and mechanisms. *Curr. Opin. Neurobiol.* **14**, 675–684 (2004).
- Lopez-Barneo, J., Darlot, C., Berthoz, A. & Baker, R. Neuronal activity in prepositus nucleus correlated with eye movement in the alert cat. *J. Neurophysiol.* **47**, 329–352 (1982).
- McFarland, J.L. & Fuchs, A.F. Discharge patterns in nucleus prepositus hypoglossi and adjacent medial vestibular nucleus during horizontal eye movement in behaving macaques. *J. Neurophysiol.* **68**, 319–332 (1992).

10. Aksay, E., Baker, R., Seung, H.S. & Tank, D.W. Anatomy and discharge properties of pre-motor neurons in the goldfish medulla that have eye-position signals during fixations. *J. Neurophysiol.* **84**, 1035–1049 (2000).
11. Seung, H.S. How the brain keeps the eyes still. *Proc. Natl. Acad. Sci. USA* **93**, 13339–13344 (1996).
12. Machens, C.K., Romo, R. & Brody, C.D. Flexible control of mutual inhibition: a neural model of two-interval discrimination. *Science* **307**, 1121–1124 (2005).
13. Singh, R. & Eliasmith, C. Higher-dimensional neurons explain the tuning and dynamics of working memory cells. *J. Neurosci.* **26**, 3667–3678 (2006).
14. Seung, H.S., Lee, D.D., Reis, B.Y. & Tank, D.W. Stability of the memory of eye position in a recurrent network of conductance-based model neurons. *Neuron* **26**, 259–271 (2000).
15. Koulakov, A.A., Raghavachari, S., Kepecs, A. & Lisman, J.E. Model for a robust neural integrator. *Nat. Neurosci.* **5**, 775–782 (2002).
16. Goldman, M.S., Levine, J.H., Major, G., Tank, D.W. & Seung, H.S. Robust persistent neural activity in a model integrator with multiple hysteretic dendrites per neuron. *Cereb. Cortex* **13**, 1185–1195 (2003).
17. Anastasio, T.J. The fractional-order dynamics of brainstem vestibulo-oculomotor neurons. *Biol. Cybern.* **72**, 69–79 (1994).
18. Major, G., Baker, R., Aksay, E., Seung, H.S. & Tank, D.W. Plasticity and tuning of the time course of analog persistent firing in a neural integrator. *Proc. Natl. Acad. Sci. USA* **101**, 7745–7750 (2004).
19. Maass, W., Joshi, P. & Sontag, E.D. Computational aspects of feedback in neural circuits. *PLOS Comput. Biol.* **3**, e165 (2007).
20. Aksay, E. *et al.* Functional dissection of circuitry in a neural integrator. *Nat. Neurosci.* **10**, 494–504 (2007).
21. Cannon, S.C., Robinson, D.A. & Shamma, S. A proposed neural network for the integrator of the oculomotor system. *Biol. Cybern.* **49**, 127–136 (1983).
22. Goldman, M.S. Memory without feedback in a neural network. *Neuron* **61**, 621–634 (2009).
23. Miri, A., Daie, K., Burdine, R.D., Aksay, E. & Tank, D.W. Regression-based identification of behavior-encoding neurons during large-scale optical imaging of neural activity at cellular resolution. *J. Neurophysiol.* **105**, 964–980 (2011).
24. McLean, D.L., Fan, J., Higashijima, S., Hale, M.E. & Fetcho, J.R. A topographic map of recruitment in spinal cord. *Nature* **446**, 71–75 (2007).
25. Weiler, N., Wood, L., Yu, J., Solla, S.A. & Shepherd, G.M. Top-down laminar organization of the excitatory network in motor cortex. *Nat. Neurosci.* **11**, 360–366 (2008).
26. Higashijima, S., Mandel, G. & Fetcho, J.R. Distribution of prospective glutamatergic, glycinergic and GABAergic neurons in embryonic and larval zebrafish. *J. Comp. Neurol.* **480**, 1–18 (2004).
27. Dasen, J.S. & Jessell, T.M. Hox networks and the origins of motor neuron diversity. *Curr. Top. Dev. Biol.* **88**, 169–200 (2009).
28. Pastor, A.M., de la Cruz, R.R. & Baker, R. Eye position and eye velocity integrators reside in separate brainstem nuclei. *Proc. Natl. Acad. Sci. USA* **91**, 807–811 (1994).
29. Arrenberg, A.B., Del Bene, F. & Baier, H. Optical control of zebrafish behavior with halorhodopsin. *Proc. Natl. Acad. Sci. USA* **106**, 17968–17973 (2009).
30. Schoonheim, P.J., Arrenberg, A.B., Del Bene, F. & Baier, H. Optogenetic localization and genetic perturbation of saccade-generating neurons in zebrafish. *J. Neurosci.* **30**, 7111–7120 (2010).
31. Escudero, M., de la Cruz, R.R. & Delgado-García, J.M. A physiological study of vestibular and prepositus hypoglossi neurones projecting to the abducens nucleus in the alert cat. *J. Physiol. (Lond.)* **458**, 539–560 (1992).
32. Aksay, E., Baker, R., Seung, H.S. & Tank, D.W. Correlated discharge among cell pairs within the oculomotor horizontal velocity-to-position integrator. *J. Neurosci.* **23**, 10852–10858 (2003).
33. Shinoda, Y. & Yoshida, K. Dynamic characteristics of responses to horizontal head angular acceleration in vestibuloocular pathway in the cat. *J. Neurophysiol.* **37**, 653–673 (1974).
34. Anastasio, T.J. Nonuniformity in the linear network model of the oculomotor integrator produces approximately fractional-order dynamics and more realistic neuron behavior. *Biol. Cybern.* **79**, 377–391 (1998).
35. Aksay, E. *et al.* History dependence of rate covariation between neurons during persistent activity in an oculomotor integrator. *Cereb. Cortex* **13**, 1173–1184 (2003).
36. Debowy, O. & Baker, R. Encoding of eye position in the goldfish horizontal oculomotor neural integrator. *J. Neurophysiol.* **105**, 896–909 (2011).
37. Sklavos, S., Porrill, J., Kaneko, C.R. & Dean, P. Evidence for wide range of time scales in oculomotor plant dynamics: implications for models of eye-movement control. *Vision Res.* **45**, 1525–1542 (2005).
38. Kinkhabwala, A. *et al.* A structural and functional ground plan for neurons in the hindbrain of zebrafish. *Proc. Natl. Acad. Sci. USA* **108**, 1164–1169 (2011).
39. McLean, D.L., Masino, M.A., Koh, I.Y., Lindquist, W.B. & Fetcho, J.R. Continuous shifts in the active set of spinal interneurons during changes in locomotor speed. *Nat. Neurosci.* **11**, 1419–1429 (2008).
40. Goldberg, J.M. & Fernandez, C. Physiology of peripheral neurons innervating semicircular canals of the squirrel monkey. I. Resting discharge and response to constant angular acceleration. *J. Neurophysiol.* **34**, 635–660 (1971).
41. Miles, F.A. & Braitman, D.J. Long-term adaptive changes in primate vestibuloocular reflex. II. Electrophysiological observations on semicircular canal primary afferents. *J. Neurophysiol.* **43**, 1426–1436 (1980).
42. Sussillo, D. & Abbott, L.F. Generating coherent patterns of activity from chaotic neural networks. *Neuron* **63**, 544–557 (2009).
43. Helmstaedter, M., Briggman, K.L. & Denk, W. 3D structural imaging of the brain with photons and electrons. *Curr. Opin. Neurobiol.* **18**, 633–641 (2008).
44. Beck, J.C., Rothnie, P., Straka, H., Wearne, S.L. & Baker, R. Precerebellar hindbrain neurons encoding eye velocity during vestibular and optokinetic behavior in the goldfish. *J. Neurophysiol.* **96**, 1370–1382 (2006).
45. Ma, L.H., Punnamoottil, B., Rinkwitz, S. & Baker, R. Mosaic *hoxb4a* neuronal pleiotropism in zebrafish caudal hindbrain. *PLoS ONE* **4**, e5944 (2009).
46. Huang, Z. *Membrane potential fluctuations in a neural integrator*. PhD thesis, Princeton University (2009).
47. Aksay, E., Gamkrelidze, G., Seung, H.S., Baker, R. & Tank, D.W. *In vivo* intracellular recording and perturbation of persistent activity in a neural integrator. *Nat. Neurosci.* **4**, 184–193 (2001).
48. Teramae, J.N. & Fukai, T. A cellular mechanism for graded persistent activity in a model neuron and its implications in working memory. *J. Comput. Neurosci.* **18**, 105–121 (2005).
49. Fransén, E., Tahvildari, B., Egorov, A.V., Hasselmo, M.E. & Alonso, A.A. Mechanism of graded persistent cellular activity of entorhinal cortex layer V neurons. *Neuron* **49**, 735–746 (2006).
50. Loewenstein, Y. & Sompolinsky, H. Temporal integration by calcium dynamics in a model neuron. *Nat. Neurosci.* **6**, 961–967 (2003).

ONLINE METHODS

All experiments were performed in compliance with protocols approved by the Princeton University Institutional Animal Care and Use Committee. We used 6–12 d post-fertilization (dpf) *mitfa*^{-/-} (also known as *nacre*) mutant zebrafish larvae ranging in length from 4.0 to 4.8 mm for all experiments. For functional imaging, eye tracking and targeted electrical recording, we used previously described techniques²³.

Functional inactivation. Zebrafish (5–6 dpf) were transgenic for a combination of transgenes: *Et(E1b:Gal4-VP16)s1101t*, *Tg(UAS:NpHR-mCherry)s1989t*, *Tg(UAS:Kaede)s1999t*. Wild type refers to siblings of NpHR expressors that potentially expressed Gal4 and Kaede. Animals were mounted in agarose in a 35-mm dish and the agarose was removed around the eyes. An optical fiber 200 μ m in diameter was placed above the caudal hindbrain to activate NpHR (633 nm, 50 mW mm⁻²). Animals were imaged at 20–30 frames per s under infrared illumination. Eye tracking was performed using a custom LabView program that detected saccades and triggered fiber illumination 1 s after half of the saccades (both ipsiversive and contraversive). Only zebrafish that showed a high frequency of saccades in both directions were used. Experiments were not performed in the dark, as scattered light from the fiber sometimes triggered saccades. Instead, a white backlight was used in addition to the infrared light to reduce the salience of the fiber light. We fit 400-ms segments of eye traces using linear regression to measure eye velocity for plots of eye velocity versus eye position. Control measurements of eye stability in the absence of illumination revealed no significant difference ($P = 0.41$, $n \geq 8$, Student's *t* test) between NpHR expressors and wild types.

Data analysis. All analysis was completed in Matlab v.7.8 or 7.10 (Mathworks). We identified somata corresponding to eye position- and ipsiversive velocity-encoding neurons from fluorescence image time series using previously described methods²³. ROI time series were calculated as the average of pixel time series for all included pixels. Eye position correlation, c_p , and ipsiversive velocity correlation, c_v , for each somata were defined as the Pearson correlation coefficient between the ROI time series and CIRF-convolved eye position and CIRF-convolved ipsiversive velocity, respectively. The significance threshold used in cell identification was set empirically so that identified somata had c_p ranging below 0.5 for some somata. This ensured that all somata with $c_p > 0.5$ were likely identified. The cellular response index, *RI*, was defined as

$$RI = \frac{1}{1 + \left| \frac{c_v}{c_p} \right|}$$

Response indices were calculated for somata for which either $c_p > 0.5$ or $c_v > 0.5$. Response indices were calculated from firing rate data using the same formula, but with c_p and c_v defined using firing rate and unconvolved eye position and ipsiversive velocity measurements. Saccade identification and STA generation are described elsewhere²³. We reiterate here that the data inclusion criteria employed ensured that included saccades had reasonably uniform sizes and preceding histories, as is indicated by measurements of the distribution of eye positions surrounding included saccades. For each STA response, we calculated the coefficient of variation for eye positions immediately preceding (mean from 400 to 300 ms before) and following (mean from 500 to 600 ms after) included saccades. For all ipsiversive STAs, the mean coefficient of variation was 0.26 for pre-saccadic eye positions and 0.14 for post-saccadic eye positions. For all contraversive STAs, the mean coefficient of variation was 0.18 for pre-saccadic eye positions and 0.16 for post-saccadic eye positions. Only 1.7% of included saccades did not cross the center of gaze. STA fluorescence responses and firing rates were convolved with a 200-ms box filter before subsequent analysis.

A deconvolution-based approach was used to calculate firing rate estimates for optically recorded cells. To do so, we first estimated CIRFs for cells²³ for which $c_p > 0.5$ ($n = 455$ position cells, this eliminates cells that may not have strong persistent activity during fixations). Confidence intervals (Matlab function *confint*) ranging between 0 and 100% in width were calculated for the CIRF τ estimate from the fit to populate a distribution representing this estimate. This method may systematically underestimate the CIRF τ for cells whose fluorescence has not completely decayed before subsequent saccades. However, we expect this underestimation

to have a minimal effect on firing rate estimation, as the median CIRF τ was less than the mean saccade frequency of ~ 10 s (ref. 23) for 94% of position cells. Deconvolutions (Matlab function *deconv*) and convolutions (Matlab function *conv*) were performed with STAs padded on either end with 5-s-long stretches of zeros using a 5-s-long stretch of an exponential decay of a given CIRF τ .

Persistence time estimates were made for cells for which $R^2 > 0.5$ for the fit to estimate CIRF τ (416 of 455 cells) according to the following four steps, which were repeated 1,000 times for each cell (Supplementary Fig. 3). First, ipsiversive and contraversive STA fluorescence responses were deconvolved with a CIRF defined by a τ chosen randomly from that cell's CIRF τ estimate distribution, generating firing rate estimates. Second, these estimates were used to define the possible range of the baseline null value to which the firing rate decays after saccades in either direction. The lower bound for the null value was estimated as the mean of the ipsiversive firing rate estimate between 1 and 2 s before the saccade time. The upper bound was estimated as the average of the means of ipsiversive and contraversive STA firing rate estimates 4–4.5 s following the saccade time (Supplementary Fig. 3). These bounds were chosen because they account for the possibility that neurons may be hyperpolarized below firing threshold after contraversive saccades. Third, a null value was chosen randomly from a uniform distribution of values between the bounds calculated in the previous step. Lastly, $Ae^{-t/\tau}$ was fit to the ipsiversive STA firing rate estimate from 1–4.5 s following saccade time after subtracting off the null value. The decay time τ from this fit is an estimate of the persistence time. Confidence intervals ranging between 0 and 100% in width were calculated for the persistence τ estimate to populate a distribution representing the estimate. These estimate distributions from all 1,000 iterations were collected into one distribution that characterizes the persistence time for a given cell. We defined the middle 99% of this collective distribution as a cell's persistence time range. Negative persistence time ranges, indicating a firing rate rising during fixation, were obtained for a fraction of optically recorded cells (50 of 416). These cells and cells for which persistence time ranges straddled 0 (49 of 416) were excluded from further analysis. The persistence time distributions for individual larvae shown in Figure 4d were populated with the median of persistence time distributions for cells with positive persistence time ranges. Fractional change in fluorescence during fixation was calculated for these same cells. It was defined as the fractional change between the mean of the first 512 ms and the last 512 ms of the segment of the STA firing-rate estimate used for persistence time estimation.

Given that deconvolution of fluorescence can result in an amplification of noise that is unrelated to the firing rate, we developed an alternative method for persistence time estimation that circumvented this undesirable effect. We calculated persistence time distributions for cells as described above a second time, but, in the last step of each iteration, we fit the function below to the ipsiversive STA fluorescence. STA fluorescence responses were fit with a model of fluorescence that would result from a firing profile consisting of an initial burst followed by an exponential decay during fixation. The fluorescence, $f(t)$, resulting from a decaying firing rate, $r(t)$, will be given by the convolution of the firing rate with the CIRF so that

$$\begin{aligned} r(t) &= ae^{-t/\tau} + c \\ f(t) &= \frac{1}{T} \int_0^t dt' r(t') e^{-(t-t')/T} \\ &= \frac{a\tau}{(\tau - T)} (e^{-t/\tau} - e^{-t/T}) + c(1 - e^{-t/T}) \end{aligned}$$

where T is the time constant of the CIRF. Given that the fluorescence at time $t = 0$ also depends on the firing rate in the past, an extra term must be included that accounts for the fluorescence resulting from past activity, so that the fluorescence during a fixation is given by

$$f(t) = \frac{a\tau}{(\tau - T)} (e^{-t/\tau} - e^{-t/T}) + c(1 - e^{-t/T}) + f(0)e^{-t/T}$$

The parameters a and τ can be estimated by fitting the STA fluorescence with this function at some time after the end of the burst. Typical bursts lasted for 100–500 ms; thus, fits began 1 s after the saccade. The parameter c , representing the null value, was held fixed at the randomly selected level during each fit.

To determine whether cellular persistence time distributions differed statistically in individual larvae, we tested the null hypothesis that the distributions for

a given larvae had equivalent medians using the nonparametric Kruskal-Wallis test (Matlab function `kruskalwallis`). Because persistence time distributions are not populated by independent measurements, the test was not performed directly on these distributions. Instead, we first determined approximately how many independent measurements were present in the segment of the ipsiversive STA firing rate estimate used for persistence time estimates. This was done by iteratively downsampling the residuals of an exponential fit to this segment until serial correlation between adjacent measurements was negligible. This method involved the following steps. First, for all cells in the dataset, we fit the segment of the ipsiversive STA firing rate estimate used for persistence time estimates with $Ae^{-t/\tau}$, generating a residual time series. Second, for all cells in the dataset, we similarly fit and generated residuals from 500 random permutations of this segment. Third, for each cell, we calculated the serial correlation for the residual time series from the first step. Serial correlation was measured for a sequence of residuals $x = x_1, x_2, \dots, x_n$, by calculating the Pearson correlation between x_1, x_2, \dots, x_{n-1} , and x_2, x_3, \dots, x_n . Fourth, we calculated the serial correlation similarly for 1,000 random permutations of this residual time series. Fifth, we calculated the fraction of the 1,000 correlation measurements from the fourth step that were larger than the correlation measurement from the third step. Sixth, we repeated the calculations from steps 3–5 for each of the residual time series generated in the second step. The resulting 500 values define a cell-specific empirical distribution for the fractions calculated in the fifth step under a null hypothesis of no serial correlation. Seventh, we calculated a P value for the fraction calculated in the fifth step assuming a two-tailed test against the null distribution generated in step 6, $2(0.5 - |\text{fraction of the empirical null distribution less than the result of step 5} - 0.5|)$. The use of a two-tailed test here makes the test sensitive to both correlation and anti-correlation. Eighth, we repeated steps 3–7 for all cells in the dataset and calculated the fraction of P values for all cells from the seventh step that fell below 0.3. Finally, we downsampled the residuals from the first and second steps to half the previous sampling frequency (Matlab function `downsample`) and repeated steps 3–8.

In the absence of serial correlation (including anti-correlation), the fraction calculated in step 8 should equal ~0.3. We observed that, as the time series were progressively downsampled, this fraction approached and then plateaued at ~0.3. Serial correlation was deemed negligible when this fraction first fell below 0.3. At this point, 15 samples remained. We performed the Kruskal-Wallis test using 15 random samples from each cell's persistence time distribution.

Somal position was defined using the ROI centroid. Cell positions were measured in distances caudal of the Mauthner cell soma, dorsal of the medial longitudinal fasciculus and lateral of the midline. For the plots shown in **Figure 6b,c**, cell pairs were grouped based on pairwise distance into bins divided at 10, 20, 30, 40, 50 and 60 μm . For the plots in **Figure 7b,c,e** and **Supplementary Figure 7b**, bins were divided at -40, -24, -8, 8, 24 and 40 μm . For the plots in **Figure 7f** and **Supplementary Figure 7a**, divisions were made at -30, -18, -6, 6, 18 and 30 μm . Directional distances were calculated by subtracting the position of one cell of a pair, cell 2, from the other, cell 1, where cell 1 was the cell whose value was used in the numerator when calculating response index or persistence time ratios. Group means were plotted as error bars representing the mean \pm s.e.m. versus the mean pairwise distance for each cohort. Outlying ratios were eliminated by including only values between the 2.5th and 97.5th percentile ratio values. Although data was binned for the purpose of plotting, correlation coefficients quoted for data presented in

Figures 6 and 7 and Supplementary Figure 7 were calculated from individual data points. P values were calculated from two-tailed Student's t tests.

Previously described³² simultaneous firing-rate measurements from pairs of adult goldfish hVPNI neurons were re-analyzed to extract persistence time estimates. Segments of firing-rate time series were used in calculating STA firing rates if they corresponded to a fixation lasting more than 4.5 s following the time of the saccade and if the average eye position from 0.5 to 1 s following the saccade fell in the top quartile of the distribution of such values for fixations following both ipsiversive and contraversive saccades. This second criteria focused the measurement on data collected during fixations more equivalent to those in larval zebrafish that largely saccade back and forth between positions near the extremes of their eye position range. The firing rate corresponding to the center of gaze was estimated as the y intercept of a linear function best-fit in the least-squares sense to the relation between firing rate and eye position. This null value was subtracted off the STA firing rate, and the function $Ae^{-t/\tau}$ was fit to the result. τ from this fit was used as the persistence time estimate. Percent differences for pairs of persistence times were computed as their absolute difference divided by their mean. One cell pair out of seven was excluded from percent difference calculation because one cell of the pair yielded a negative persistence time. Only zebrafish neurons having exclusively positive persistence time ranges were used to estimate pairwise percent differences.

Simulations. Network simulations used the linear system

$$\tau_r \frac{dr_i}{dt} + r_i = \sum_{j=1}^N w_{ij} r_j$$

where r_i represents the firing rate of neuron i and w_{ij} represents the weight of the connection from neuron j to neuron i . All network simulations were generated using the fourth-order Runge-Kutta method with 0.002-s time steps. τ_r was set to 1 s, the same value assumed based on experimental results for adult goldfish hVPNI neurons in reference 20, and $N = 50$. All rates were set to 1 at the first time point.

The weight matrix for the uniformly detuned line attractor network was generated as the outer product of two random vectors scaled uniformly so that the persistence time of simulated units was ~5 s, approximately the median value for optically recorded cells for which we calculated persistence times. The weight matrix for the feedback network with multiple stable dimensions was constructed by setting the weights between neurons equal to $\max\{0, 11 - |i - j|\}$ for $i \neq j$ (this effects a proximity bias to the connectivity weights) and 0 for $i = j$ (no autapses). Entries were then divided by the sum of all entries in their respective columns and scaled by $0.185 + 0.985 (i/N)$. The constants in this expression were chosen empirically to create a distribution of persistence times qualitatively similar to those experimentally observed. The weight matrix for the asymmetric network with a feedforward bias was constructed by setting the weights between neurons equal to $\max\{0, 20 - (j - i)\}$ for $i < j$, $\max\{0, 10 - (i - j)\}$ for $i > j$, and 0 for $i = j$. Entries were then divided by the sum of all entries in their respective columns and scaled by $0.21 + 1.11 (i/N)$. Collectively, these network simulations illustrate three ways in which spatially organized heterogeneity in firing dynamics could be generated. In future work, a more comprehensive approach could be pursued in which possible circuit and synaptic properties are determined by fitting models directly to data.